3D reduced graphene oxide aerogel-mediated Z-scheme photocatalytic system for highly efficient solar-driven water oxidation and removal of antibiotics

Qinqin Liu[a], Jiyou Shen[a], Xiaofei Yang[a,b,c,*], Tierui Zhang[d], Hua Tang[a,*]

[a] School of Materials Science and Engineering, Jiangsu University, Zhenjiang, 212013, PR China
[b] College of Science, Nanjing Forestry University, Nanjing 210037, PR China
[c] State Key Laboratory of Photocatalysis on Energy and Environment, Fuzhou University, Fuzhou, 350002, PR China
[d] Key Laboratory of Photochemical Conversion and Optoelectronic Materials, Technical Institute of Physics and Chemistry, Chinese Academy of Sciences, Beijing, 100190, PR China

ARTICLE INFO

ABSTRACT

The construction of natural photosynthesis-inspired Z-scheme tandem system has been considered as a promising strategy to fulfill efficient electron-hole separation and charge transportation in composite photocatalysts, providing a unique opportunity to achieve improved solar-driven photocatalytic water splitting performance superior to conventional heterojunctions. The presence of an ideal electron mediator is critical to promote effective electron transfer in Z-scheme semiconductor photocatalytic systems. Herein, for the first time, we report the fabrication of $CeVO_4$/three-dimensional (3D) reduced graphene oxide (RGO) aerogel/$BiVO_4$ ternary composites and their use as photocatalysts for visible-light-driven water oxidation and tetracycline (TC) degradation. As-prepared hybrid materials exhibit well-organized heterostructures where two vanadates with different dimensional features are surrounded by 3D aerogel networks. Under visible light irradiation, the optimal composite material revealed highly improved photocatalytic activity both in oxygen evolution from water splitting and TC degradation. The enhancement in photocatalytic efficiency is assumed to come from illuminated Z-scheme $CeVO_4$/3D RGO/$BiVO_4$ configuration, in which conductive 3D RGO aerogel functions as an effective electron mediator and builds the bridge between two vanadates, offering a tandem channel for more efficient charge transfer in two semiconductors. This work may provide a new clue for the design of all-solid-state Z-scheme composite photocatalytic materials in energy and environmental applications.

1. Introduction

The past few years have witnessed an overwhelming amount of research on composite photocatalysts for applications in energy conversion and environmental remediation, due to the fact that the application of a single-component photocatalyst is majorly limited by its light-harvesting property in the visible light region, unmatched band structure and redox potential [1–4]. Inspired by natural photosynthesis, Z-scheme composite photocatalysts have attracted more attention, particularly in the field of solar-to-fuel conversion and storage [5–7]. Compared with conventional heterojunction-type composite photocatalysts, Z-scheme photocatalytic systems demonstrate superior efficiency owing to its specific tandem configuration and suitable redox potentials for water splitting [8,9]. A typical Z-scheme composite photocatalytic system consists of two semiconductors and an electron

mediator, of which the electron mediator plays key roles in determining the efficiency of electron-hole separation and charge transfer, and predominantly affecting water splitting performance [10].

Early researches are mainly focused on the introduction of a variety of acceptor/donor (A/D) pairs as electron mediators for the connection of two semiconductors to form different Z-scheme composite photocatalytic systems [11]. However, ionic A/D pairs such as Fe^{3+}/Fe^{2+}, IO_3^-/I^- only can be utilized in liquid phase photocatalytic reactions [12]. Furthermore, A/D pairs are chemically unstable under light illumination, fatal backward reactions are generally involved that may cause severe negative effects on photogenerated carriers [13]. The replacement of ionic A/D pairs by solid-state electron mediators has emerged as an alternative way to establish a Z-scheme composite photocatalytic systems. Up to now, mainly two kinds of materials, noble metal and reduced graphene oxide (RGO), have proven to be promising

solid-state electron mediators for shuttling photogenerated charges [14]. Sheet-like RGO materials demonstrate advantages in specific lamellar structure, chemical stability, morphological diversity and cost-effective preparation superior to noble metals, affording more active sites and boosting the catalytic reactions on the surface. Amal et al. [15] reported the use of RGO as an electron mediator in a Z-scheme composite photocatalyst, in which oxygen-producing photocatalyst $BiVO_4$ was bridge-connected with hydrogen-evolving photocatalyst $Ru/SrTiO_3$ by highly conductive RGO sheets. Kudo et al. [16] developed a Z-scheme photocatalytic water splitting system consisting of $CuGaS_2/Pt$ and $RGO-TiO_2$ composites by using a RGO electron mediator. The above study suggested that the employment of RGO as an electron mediator in a Z-scheme system enabled a faster electron-hole separation and improved photocatalytic activity. The use of RGO as an effective electron mediator can be readily extended to design and synthesize novel semiconductor-based Z-scheme composite photocatalytic systems for applications in energy and environmental science [17–19].

Vanadates possessing narrow band gap and high chemical stability have been considered as prospective visible-light driven photocatalysts [20], among which $BiVO_4$ is a most commonly oxygen-evolving photocatalyst owing to its suitable band structure and valance band potential [21]. However, its catalytic efficiency is not satisfactory due to a fast recombination of photogenerated carriers. $CeVO_4$ is another typical vanadate, utilizing $CeVO_4$ as a photocatalyst has been rare since it possesses unmatched redox potentials for water splitting [22]. Taking theoretical redox potentials into consideration, the generation of a $BiVO_4/CeVO_4$ heterojunction is beneficial for the separation of photogenerated carriers. As stated above, the integration of RGO sheets into a semiconductor-based photocatalyst may accelerate the electron-hole separation and boost charge transfer. Superior to 2D RGO sheets, 3D RGO nanostructures reveal interconnected networks with highly improved surface area and more active sites, it is presumable that the assembly of vanadate semiconductors into 3D RGO nanostructures may lead to the formation of well-defined vanadate/3D RGO heterostructures [23]. In this work, we demonstrate a synthetic approach to fabricate a novel $BiVO_4/3D$ RGO aerogel/$CeVO_4$ Z-scheme composite photocatalyst, where $BiVO_4$ is employed as an oxygen-generating photocatalyst and $CeVO_4$ is introduced as a co-catalyst, while 3D RGO aerogels work as an electron mediator. To the best of our knowledge, it is for the first time that vanadate/3D RGO ternary composite photocatalyst has been reported for all-solid-state Z-scheme photocatalysis. The ternary $BiVO_4/3D$ RGO aerogel/$CeVO_4$ composite photocatalyst has the potential to meet all requirements in photocatalysis including visible light adsorption, electron-hole separation and redox potentials for catalytic reactions. The approach can be applied to synthesize a variety of 3D RGO aerogel-mediated Z-scheme photocatalytic systems, the information provided in this study allows us to reveal electron transfer pathway in Z-scheme-type photocatalysis.

2. Experimental

2.1. Preparation

Graphene oxide (GO) was fabricated by modified Hummers method [24]. In a typical synthesis of $BiVO_4/3D$ RGO aerogel/$CeVO_4$ ternary composites, GO aqueous solution (30 mL, 3 mg/mL) was treated with ultrasonic for 3 h. After that, 33 mg $Ce(NO_3)_3 \cdot 6H_2O$, 37 mg $Bi(NO_3)_3 \cdot 5H_2O$ and 18 mg NH_4VO_3 was dissolved in 5 mL H_2O, 10 mL HNO_3 (2 mol/L) and 10 mL H_2O, respectively. Dissolved Bi and Ce solutions were added simultaneously into GO solution under magnetic stirring, followed by the addition of NH_4VO_3 solution into the above mixed solutions. Subsequently $NH_3 \cdot H_2O$ was utilized to adjust pH value to 8.8. The resultant slurry was transferred to a Teflon-lined autoclave and heated at 180℃ for 20 h. Afterwards, deionized water dialysis was carried out for 3 days in order to remove the impurities. Finally, as-prepared hydrogels were freezing dried to form aerogels. $BiVO_4/3D$

RGO aerogel/$CeVO_4$ ternary composites with different molar ratios of $BiVO_4/CeVO_4$ were synthesized using the above procedure by varying the mass ratio of raw materials. The samples prepared with molar ratios of $BiVO_4/CeVO_4$ = 10: 1, 5: 1, 2: 1, 1 : 1 and 1: 2 are denoted as BGC10, BGC 5, BGC 2, BGC1 and BGC0.5, respectively. The BGC ternary composites by using a fixed molar ratio of $BiVO_4/CeVO_4$ (1:1) under different hydrothermal conditions were also synthesized for comparison.

2.2. Characterization

X-ray diffraction (XRD) data were obtained by a Rigaku D/Max2500 X-ray powder diffractometer. X-ray photoelectron spectroscopy measurements were conducted using a Thermo ESCALAB MKII. The morphological features of the products were observed using scanning electron microscopy (SEM, JSM-7001F) and transmission electron microscopy (TEM, JEM-2100). The UV–vis diffuse reflectance spectra were measured by UV–vis spectrophotometer (DRS, UV-2550) using $BaSO_4$ as the reference. N_2 adsorption/desorption performance was taken on the high speed automatic surface and porosity analyzer (TriStar II 3020). The fluorescence (FL) spectra were obtained by QuantaMasterTM 40 steady-state measurement system and the excitation wavelength was 325 nm. The electron spin resonance (ESR) spectra were performed using a Bruker model A300 spectrometer under irradiation, in which 5, 5-dimethyl-l-pyrroline N-oxide (DMPO) was used as spin-trapping reagent.

2.3. Photocatalytic test

2.3.1. TC degrading

The photocatalytic performances of as-prepared products were tested by degrading TC aqueous solution (20 mg/L) under irradiation of a Xenon lamp (CHF-XM-500W). The test was performed at room temperature, 50 mg photocatalysts were added into 100 mL TC solution, then the dark reaction 60 min was used to achieve the adsorption equilibrium. At given time intervals, 3 mL solution was sampled during the photocatalytic experiment. The absorbance of TC solution was measured by Shimadzu UV–vis spectrophotometer at 358 nm.

2.3.2. Oxygen evolution

Photocatalytic O_2 evolution was carried out in a sealed double-layered flask equipped with a water-cooling system using an oxygen probe (PreSens Precision Sensing GmbH, Fibox 3 fiber optic oxygen transmitter). The temperature of the whole reaction system was almost constant. For each O_2 generating reaction, 300 mg catalysts were added into 100 mL deionized water via ultrasonic dispersion and 1 g $AgNO_3$ was used as sacrificial agent. The mixture was then degassed to remove oxygen by N_2 in the dark. The light source adopts LED light. The photocatalytic O_2 evolution efficiency was calculated by measuring the evolved O_2 produced from water under regular irradiation time intervals.

2.4. Photoelectrochemical measurements

The photocurrents and electrochemical impedance spectroscopy (EIS) of the catalysts were tested using an electrochemical workstation (CHI–660E, Shanghai, China) under irradiation of 500 W Xe lamp. Catalysts, ethanol and ethylene glycol were mixed and dip-coated on the ITO film to prepare ITO/sample electrode. 0.1 M $NaNO_3$ solution was chosen as the supporting electrolyte.

3. Results and discussion

The formation process from precursors to $BiVO_4/3D$ RGO hydrogel/$CeVO_4$ hybrids and final $BiVO_4/3D$ RGO aerogel/$CeVO_4$ composites by combining hydrothermal synthesis and freeze drying is illustrated in Fig. 1. The zeta potential of ultrasonicated graphene oxide is
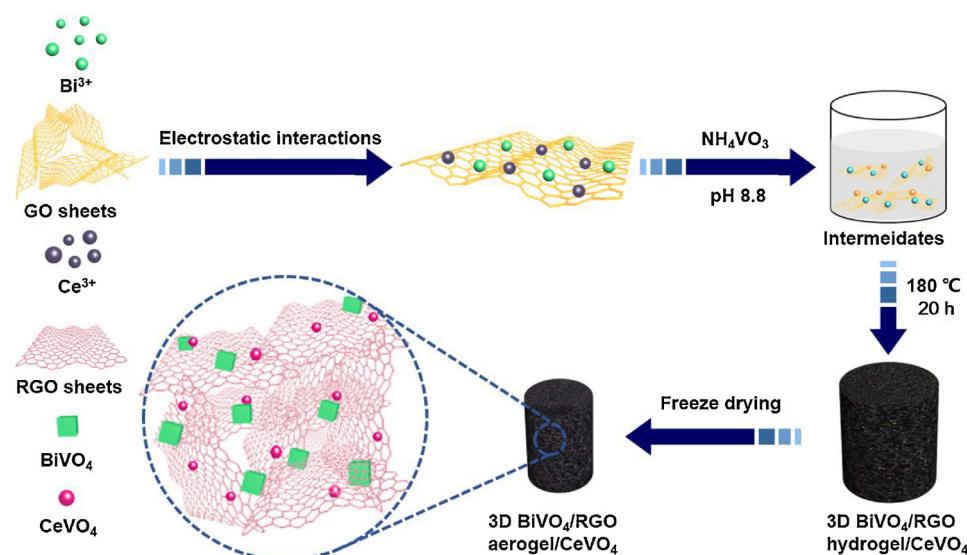
Fig. 1. Schematic illustration of the fabrication process of BiVO$_4$/RGO/CeVO$_4$ ternary composite.

determined to be -37 mV, thus postively charged Bi^{3+} and Ce^{3+} cations could be assembled on the surface of negatively charged graphene oxide sheets driven by electrostatic interactions. The addition of VO$_3^{3-}$ ions into the cation-involved suspension and the control in pH value of the mixture resulted in the formation of vanadate seed nanoparticles on ultrasonicated graphene oxide sheets. Under hydrothermal treatment, both the nucleation and growth processes of BiVO$_4$ and CeVO$_4$ are accelerated in a sealed autoclave at elevated temperature, while graphene oxide sheets with oxygen-containing residues are partially reduced and simultaneously self-assembled to build up a hydrogel network owing to hydrogen bonding and $\pi-\pi$ stacking interactions [25]. Macroscopically the hydrogel appears a damp black cylinder where vanadate nanoparticles are randomly deposited on 3D network. Upon freeze drying, the volume shrinkage occurs due to the volatilization of solvent, resulting in the generation of flexible sponge-like aerogels with interconnected 3D networks. Particulate vanadate materials with different dimensions are in-situ embedded in the reduced and confined 3D aerogel microenvironment.

In order to reveal the morphological features of the obtained heterostructured materials, microscopic study of the obtained hydrid materials was conducted by combining elemental mapping annlysis, SEM, TEM and HRTEM characterizations. For simplicity, only BiVO$_4$, CeVO$_4$ and BGC1 ternary composite were chosen for comparison. As shown in Fig. 2a and b, pristine BiVO$_4$ reveals irregular polyhedral microstructuress with smooth surfaces and highly exposed facets with an average diameter of 3 μm. While bulk CeVO$_4$ exhibits well-organized and uniformly distributed nanostructures with diameters ranging from 10 to 30 nm. Low-magnification and high-magnification SEM images of BGC1 composite shown in Fig. 2c and d confirm the formation of 3D porous heterostructures, where micro-sized BiVO$_4$ polyhedrons and CeVO$_4$ nanoparticles are both anchored on flexible RGO sheets, suggesting an intimate interfacial contact between vanadate semiconductors and sheet-like RGO materials. A deeper insight into SEM observations indicates that both the aggregations of BiVO$_4$ and CeVO$_4$ particles has been suppressed compared to that of bulk materials. Similar phenomena were also observed in other RGO-based composites in which the agglomerations of semiconductor particles were inhibited by confinement effect of large-surface-area RGO nanosheets [26]. TEM image which taken from a selected area of the BGC1 composite is shown in Fig. 2e, which further prove the presence of BiVO$_4$ microparticles, CeVO$_4$ nanoparticles and RGO sheets. Furthermore, high-resolution TEM image shown in Fig. 2f discloses a lattice spacing of 0.37 nm on the nanoparticles anchored on microsized particles, corresponding to the

(200) plane of CeVO$_4$. The spatial distribution of BiVO$_4$ and CeVO$_4$ in the composite was further characterized by elemental mapping analysis. The C, Ce, Bi, V and O elements with distinct color contrast could be observed, and distributions of these elements are almost identical to those shown in SEM image. The above microscopic study provides sufficient evidences in support of our claim that BGC ternary composites with superior interfacial contacts between vanadates and RGO aerogels are successfully fabricated.

The crystal structure of as-prepared samples was investigated by XRD and the results are shown in Fig. 3a and b. For bare BiVO$_4$, all diffraction peaks correspond to monoclinic scheelite phase of BiVO$_4$ (JCPDS 14-0688). While the peaks of bare CeVO$_4$ are in good agreement with a tetragonal structure (JCPDS 29-0398). For BGC1 ternary composite, both tetragonal CeVO$_4$ and monoclinic BiVO$_4$ are observed, the co-existence of two crystalline materials does not change diffraction peak positions of single component, implying that in-situ growth of the CeVO$_4$ and BiVO$_4$ is mutually independent. No characteristic diffraction peak of RGO is observed as the peak intensity of RGO is far below those derived from vanadate materials. No additional impurity phase is found in diffraction pattern, indicating no undesirable phase is obtained in the synthetic procedure. In terms of BGC ternary composites with different ratios of BiVO$_4$ to CeVO$_4$, the relative height of the diffraction peaks of CeVO$_4$ has a linear relationship with the ratio of BiVO$_4$ to CeVO$_4$. It is clearly shown in Fig. 3c that the crystallinity can be improved by the elevated hydrothermal temperature and prolonged hydrothermal time. A deeper insight into structural properties of as-prepared samples is revealed by Raman analysis (Fig. 3d). Bare BiVO$_4$ shows three Raman bands at 366 cm^{-1}, 757 cm^{-1} and 851 cm^{-1}, which can be assigned to asymmetric bending of VO$_4$ tetrahedrons, asymmetric V$-$O stretching mode and symmetric V$-$O stretching mode, respectively [27]. Four Raman modes of bare CeVO$_4$ located at 366 cm^{-1}, 461 cm^{-1}, 772 cm^{-1}, 846 cm^{-1} are ascribed to A$_{1g}$ deformation, B$_{2g}$ bending modes of VO$_4^{3-}$ tetrahedrons, *Eg* asymmetric and A$_{1g}$ symmetric stretching modes [28]. For graphene oxide, two characteristic bands corresponding to D and G bands were observed at 1348 and 1588 cm^{-1}, while the D band is attributed to the presence of sp^3 defects and the G band is ascribed to graphitic sp^2 hybridized carbon [29]. It is noted that the value of peak intensity ratio (I$_D$/I$_G$) is a common mean to evaluate degree of disorder and reduction of graphene. The I$_D$/I$_G$ of BGC1 composite is calculated to be 1.17, which is higher than that of GO (0.96), indicating that a partial reduction of oxygen-containing functional groups during the hydrothermal treatment. The BGC1 composite showed all Raman modes of vanadates and D, G peaks of RGO,
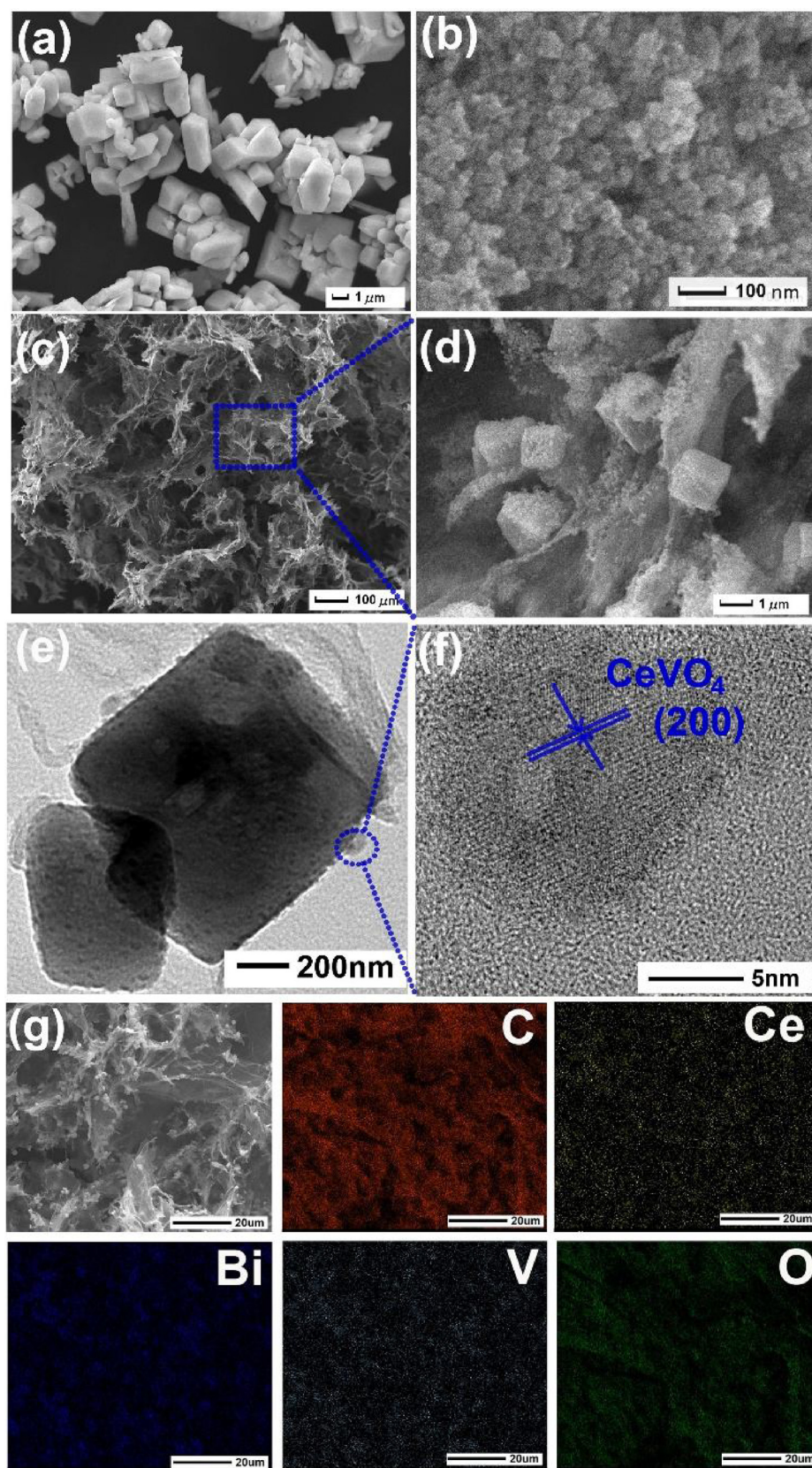
Fig. 2. SEM images of (a) BiVO₄, (b) CeVO₄, (c and d) BGC1 ternary composite, (e) TEM and (f) HRTEM images of ternary composite and (g–h) selected area for elemental mapping analysis.
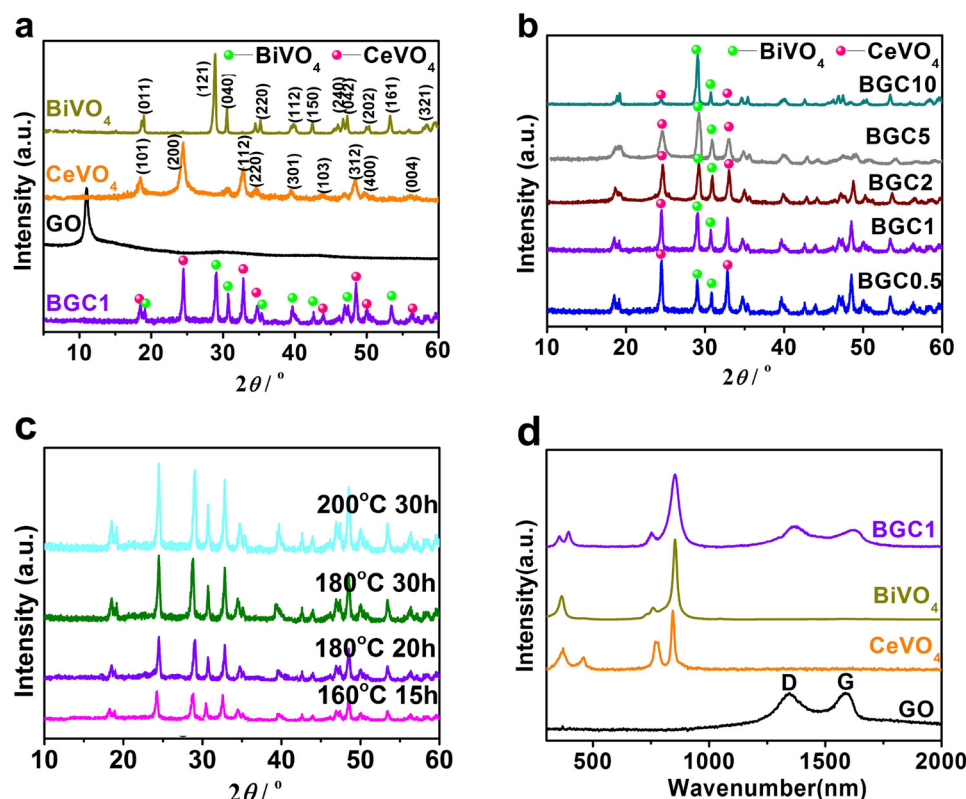
Fig. 3. Characterization of series photocatalysts: (a–c) XRD patterns, (d) Raman spectra.

indicating a complete hybridization of CeVO₄, BiVO₄ and RGO. It is also can be found that B_{1g} bending mode of VO_4^{3-} in the aerogel shows a shift towards lower wavenumber compared with that of bare CeVO₄, implying the occurrence of interaction between CeVO₄, BiVO₄ and RGO aerogel [30]. To further clarify chemical environments of the optimal BGC1 composite, XPS analysis was performed. The survey spectrum shows that Bi, Ce, V, C and O elements co-exist in the ternary composite (Fig. 4a). Fig. 4b displays that C1s can be fitted into three peaks, the main peak at 284.4 eV is attributed to sp²-hybridized carbon and the other two are hydroxyl carbon and carboxyl, respectively [31]. As for Bi 4f (Fig. 4c), two peaks centered at 160.8 eV and 165.9 eV correspond to signals of Bi $4f_{7/2}$ and Bi $4f_{5/2}$ [32]. The two peaks of Ce 3d (Fig. 4d) located at 881.6 and 886.3 eV are attributed to Ce $3d_{5/2}$ binding energy while two others centered at 900.4 and 904.2 eV correspond to Ce $3d_{3/2}$ binding energy, respectively, indicating a valence state of + 3 for Ce in the composite [22]. The V 2p peaks located at 517.8 and 524.7 eV are in accordance with the V $2p_{3/2}$ and V$2p_{1/2}$ in the BiVO₄ and CeVO₄ (Fig. 4e). The high-resolution O 1 s spectrum is shown in Fig. 4f, the peak at 530.1 eV is attributed to the O^{2-} ions at the lattice sites of the BiVO₄ or CeVO₄ while those at 531.7 eV and 532.9 eV may be related to the Ce oxides. XRD, Raman and XPS analysis results prove that BGC ternary composite is composed of monoclinic BiVO₄, tetragonal CeVO₄ and RGO aerogel, and RGO aerogel does not affect growth of crystal orientations of CeVO₄ and BiVO₄ but provides a platform where vanadate particles can grow.

The photocatalytic activities of as-prepared samples were evaluated by degrading TC under visible light irradiation, and the results are shown in Fig. 5a and b. It can be seen that the photodegradation capability over bare CeVO₄, BiVO₄ is weak, only 31% and 34% of TC are decomposed. All BGC ternary composites showed highly improved photocatalytic ability comparable to bulk BiVO₄. With an increased content of BiVO₄, the photocatalytic activitiy first increases and then decreases. The BGC1 composite demonstrated the highest photocatalytic activity, and TC was completely degraded in 60 min. Further,

the degradation reaction kinetics was studied using pseudo first order kinetic model ($\ln(C_0/C) = k_{app}t$) as the low concentration of TC, in which k_{app} is the apparent rate constant (min^{-1}) [33,34], and the results are shown in Fig. 5c and d. Apparently, linear relationship between $\ln C_0/C$ and t can been seen for all samples, indicating that the photodegradation reaction abides by pseudo-first-order kinetic equation. BGC1 composite showed the highest degradation rate and its k_{app} is 3.7 times higher than that of bare BiVO₄. The synergistic effects between BiVO₄, CeVO₄ and RGO skeletons in combination with a porous aerogel feature are assumed to be the main reason responsible for the enhanced photcatalytic performance of the BCG1 ternary composite. After that, BGC1 composite with best photocatalytic performance was chosen for the reliability test. Fig. 5e shows results of photocatalyst recycling experiments toward TC degradation, the optimal BGC1 composite still maintains a high degradation rate for TC after 5 runs. The crystal phase of the BGC1 composite after photocatalysis was characterized by XRD (shown in Fig. 5f), which is consistent with the crystal structure before the reaction. Furthermore, in practical applications, products not only need good photocatalytic property and high stability, but also require easy recovery. Bare BiVO₄ and BGC1 composite after photocatalytic experiment are recycled by a simple filtration using a 75 μm stainless steel sieve, the results are shown in insert of Fig. 5f. Aerogels can be easily recycled using this simple tool while powder samples can hardly be recycled without complicated centrifugation. This excellent retrievability of 3D composite is attributed to that the ternary composite owns 3D macroscopic aerogel structure constructed by RGO sheets [22,23,35].

3D aerogels with porous features possess large surface area and may exhibit superior absorption ability than conventional porous materials, which is proven to be beneficial to photocatalytic performance [36]. Therefore, adsorption capacities of CeVO₄, BiVO₄ and BGC composites toward TC were tested in dark, and the results are shown in Fig. 6a and b. It can be seen that the adsorption of TC over BiVO₄ or CeVO₄ became saturated after 30 min, while it took 60 min for the BGC1 composite to
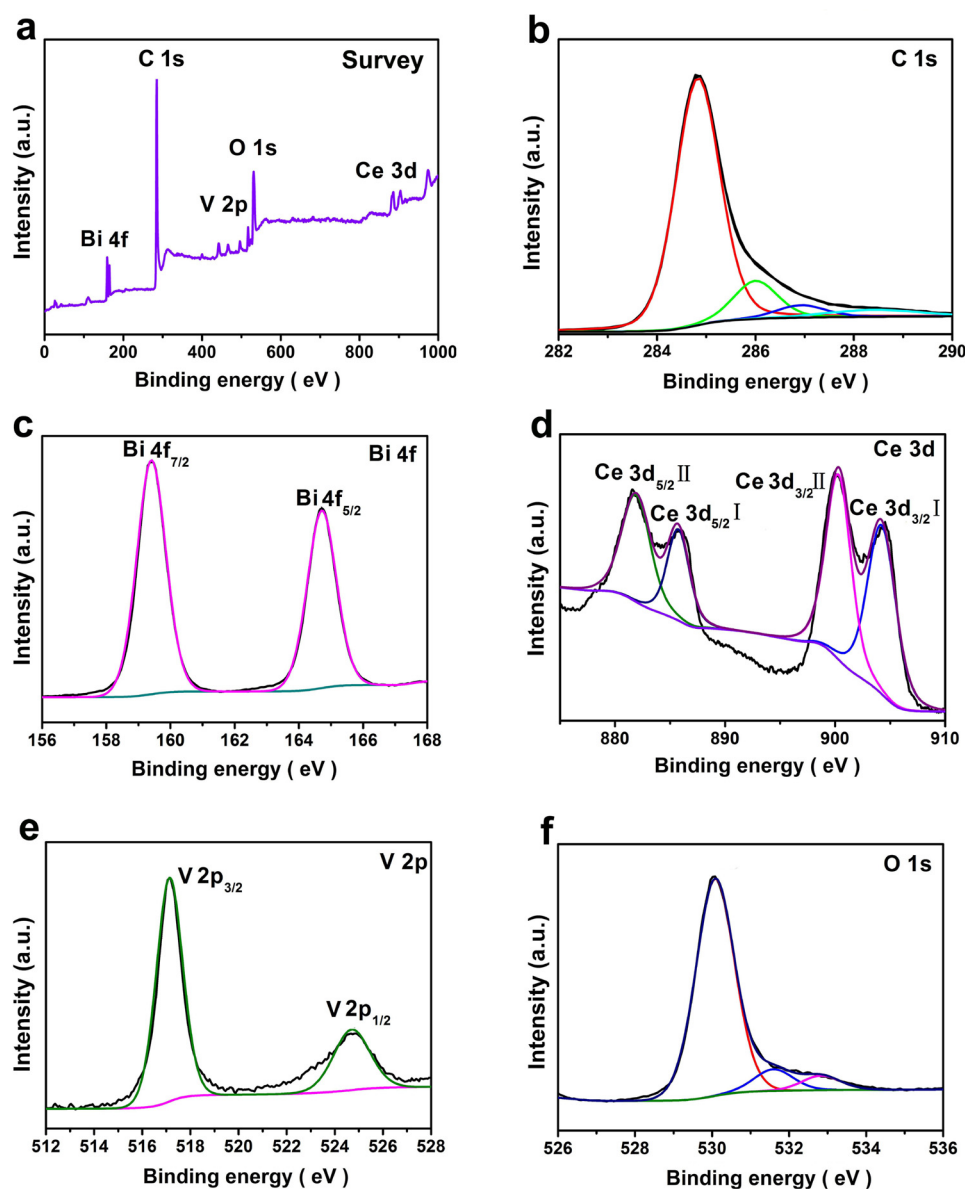
Fig. 4. XPS spectra of the BGC1 ternary composite photocatalyst.

achieve saturated. Due to the nature of 3D aerogel network, the BCG1 composite showed much higher adsorption capacity than that of $BiVO_4$ and $CeVO_4$. The TC removal efficiency reached 69% for BGC1 aerogel while the removal efficiencies over $BiVO_4$ and $CeVO_4$ were 25% and 18%, respectively. In order to determine the surface area and pore structure of $BiVO_4$, $CeVO_4$ and the BGC1 composite, nitrogen adsorption & desorption measurements with Brunauer-Emmett-Teller (BET) method were utilized and the results are shown in Fig. 6c. For the BGC1 composite, its isotherm is a typical Type IV loop, indicating the existence of mesopores and macropores [37]. There is no obvious manifestation of IV loop for bare $BiVO_4$ and $CeVO_4$. We calculated the pore-size distribution through Barrett–Joyner–Halenda (BJH) method, and the results are shown in Fig. 6d. For BGC1 composite, the pore size distribution plot shows an average pore size of 37.94 nm, while no porous structure is observed for $BiVO_4$ and $CeVO_4$ sample. The specific surface area (S_{BET}) of the aerogel is calculated to be 44.09 m^2/g, which is about 9.3 times or 6.5 times larger than those of $BiVO_4$ (4.73 m^2/g) and $CeVO_4$ (6.75 m^2/g).

Although the TC removal by the adsorption and photodegradation was conducted, the effects of dye adsorption on the total removal

efficiency are hard to be quantified, only few evidences can be obtained for the confirmation of highly efficient photodegradation of TC under light illumination. In order to further reveal the photocatalytic activity originating from the ternary BGC composites, solar-driven photocatalytic oxygen evolution performance of the obtained BGC composites was also investigated under LED illumination. The amount of evolved oxygen versus irradiation time is shown in Fig. 7a, a continuous oxygen evolution was observed for all samples. The rate of oxygen production over the BGC1 composite was 85.68 µmol/L/g, which is 2.1 faster than that generated over single-component $BiVO_4$ photocatalyst (Fig. 7b). Visible-light-driven photocatalytic oxygen evolution results excludes the effect of adsorption, which further prove that the construction of $BiVO_4$/3D RGO aerogel/$CeVO_4$ architecture can effectively improve the photocatalytic performance.

Generally solar photocatalytic performance of a photocatalyst is highly dependent on light-harvesting property in the visible region, redox potential, electron-hole separation and charge transfer efficiency [38]. Since it has been previously shown that the $BiVO_4$/3D RGO aerogel/$CeVO_4$ composite photocatalyst possesses a larger surface area which can improve the photocatalytic activity, subsequently
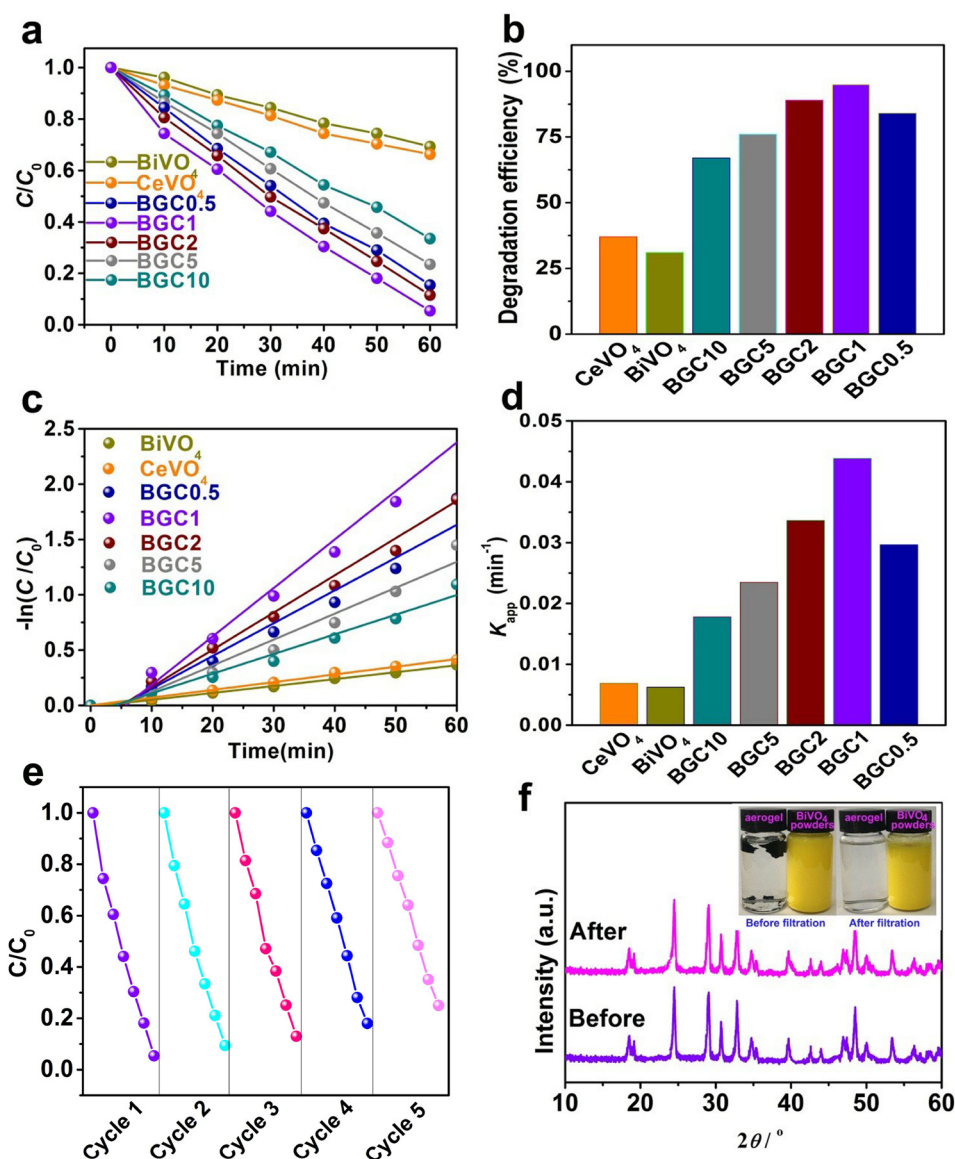
Fig. 5. (a–b) Photocatalytic degradation rate of TC under visible light irradiation; (c–d) linear transform -ln(C/C₀) of the kinetic curves of TC degradation for as-prepared catalysts; (e) recycled photocatalytic degradation experiments over the BGC1 composite (f) XRD spectra of the ternary BGC1 composite before and after the photocatalytic reaction and the insert picture is the comparison of BiVO₄ powders and BGC1 composite before and after filtration.

photocurrent, electrochemical impedance spectra (EIS) and photo-luminescence (PL) measurements were carried out. Basically higher photocurrent intensity, smaller semicircle radius and lower intensity of PL spectra imply more efficient electron-hole separation [39]. The transient photocurrents of BiVO₄, CeVO₄ and the BGC1 composite were recorded under LED irradiation with light ON/OFF every 30 s at 0.2 V, and the results are shown in Fig. 8a. The BGC1 composite showed the highest photocurrent density and its photocurrent density is 1.7 times and 2.2 times higher than those of BiVO₄ and CeVO₄. Moreover it is obvious that the semicircle radius for the BGC1 composite is smaller than that for BiVO₄ and CeVO₄ (Fig. 8b). BiVO₄ presented a strong PL emission peak around 550 nm and CeVO₄ displayed a PL emission peak around 542 nm (Fig. 8c). In comparison with BiVO₄ and CeVO₄, drastic quenching of PL intensity was observed for the BCG1 composite. Besides, the BGC1 composite exhibited the lowest PL intensity in all BGC composites with different molar ratios (Fig. 8d). The combined results of photocurrent, EIS and PL spectra offer sufficient evidences for a faster charge transportation in the obtained BiVO₄/3D RGO aerogel/CeVO₄ composite photocatalyst.

Generally, there are two pathways of photogenerated charge transfer in a photocatalytic system consisting of two semiconductors, one is the heterojunction mechanism and the other is a Z-scheme-type mechanism. Although the movement of photo-induced electrons cannot be directly observed, the pathway can be proposed through band structures and redox potentials of semiconductors, as well as types and intensities of radicals in-situ generated in the illuminated photo-catalytic system. The band structures of as-prepared samples were analyzed using UV–vis diffuse reflectance spectroscopy, while the va-lance band positions of the BiVO₄ and CeVO₄ were determined by XPS valence band spectroscopy. It is shown in Fig. 9a that both BiVO₄ and CeVO₄ semiconductors displayed similar absorption property. The ab-sorption edges of BiVO₄ and CeVO₄ are approximately 550 and 700 nm, respectively. The optical band gap of a direct semiconductor can be estimated from the following formula [40]: $\alpha(h\nu) = A(h\nu - E_g)^{1/2}$ where α, h, ν, E_g and A are absorption coefficient, plank constant, light frequency, band gap energy, and a constant, respectively. Therefore, band gaps of pure BiVO₄ and CeVO₄ are determined to be 2.43 and 1.77 eV, respectively (Fig. 9b). In comparison with bare samples, the BGC1 composite presented wide-spectrum absorbance ranging from 350 nm to 800 nm and its absorption curve was almost straight over the
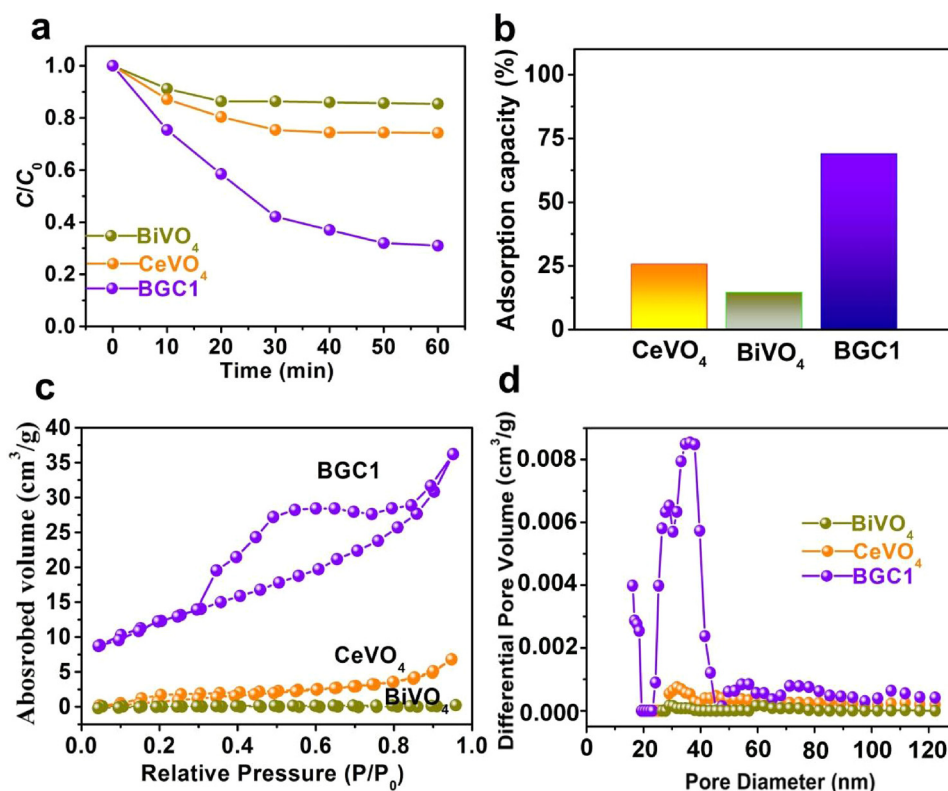
Fig. 6. (a–b) Adsorption ability toward TC over $BiVO_4$, $CeVO_4$, and the BGC1 ternary composite; (c) N_2 adsorption/desorption isotherms and (d) pore size distribution curves of $BiVO_4$, $CeVO_4$ and the BCG1 ternary composite.

whole region, indicating that the introduction of RGO aerogel into the ternary composite leads to a dramatic improvement in light-harvesting property. The valance band (VB) potentials of $BiVO_4$ and $CeVO_4$ are determined to be 2.73 eV and 1.56 eV, respectively in XPS valence band spectra (Fig. 9c). As-previous mentioned, the band gaps of $BiVO_4$ and $CeVO_4$ are calculated to be 2.43 and 1.77 eV. Thus, the conduction band (CB) potentials of $BiVO_4$ and $CeVO_4$ are deem to be 0.30 eV and −0.21 eV, respectively. The band structures of $BiVO_4$ and $CeVO_4$ are determined and the scheme is illustrated in Fig. 9d.

Different pathways of the photogenerated carriers may lead to the recombination of the holes and electrons, or accumulation of electrons and holes solely on different band positions of semiconductor materials, enabling the generation of active oxygen-containing radicals via illuminated redox reactions. Therefore, free radicals in-situ produced in the irradiated photocatalytic process is logically helpful in determining possible pathways of electron-hole separation and charge transfer

process. In order to clarify active oxygen-containing radicals produced in the TC removal, holes and radicals trapping experiments, nitroblue tetrazolium (NBT) testing as well as in-situ electron spin resonance (ESR) measurements were carried out. In radical trapping experiment, p-benzoquinone (BZQ), disodium ethylenediamine tetraacetate (Na$_2$-EDTA) and butyl alcohol (BTA) were additional added into TC degrading reaction for trapping superoxide radicals ($\cdot O_2^-$), holes (h^+), and hydroxyl radicals ($\cdot OH$), respectively [41], and the results are shown in Fig. 10a. For BGC1 composite, the degradation efficiency of TC decreased significantly when BZQ and BTA was used Na$_2$-EDTA shows weak influences on the photodegradation process. This results suggest that for $BiVO_4$, the $\cdot O_2^-$ and h^+ are the main radicals responsible for TC removal while $\cdot OH$ plays a relatively minor role. However, for $BiVO_4$, $\cdot OH$ played the vital role in the photocatalytic degrading TC. The transformation percentage of NBT are also utilized to confirm the existence or absence of $\cdot O_2^-$ during the photoreaction

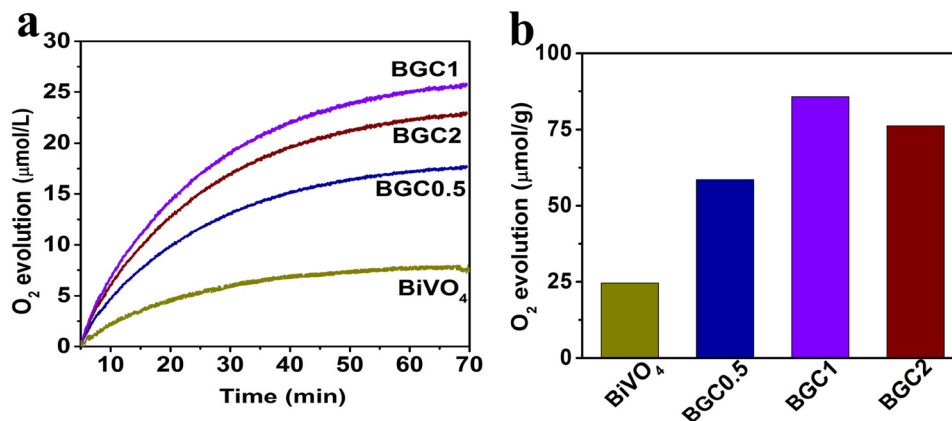**Fig. 7.** (a–b) Photocatalytic oxygen evolution performance over the $BiVO_4/RGO/CeVO_4$ ternary composites and bare $BiVO_4$.
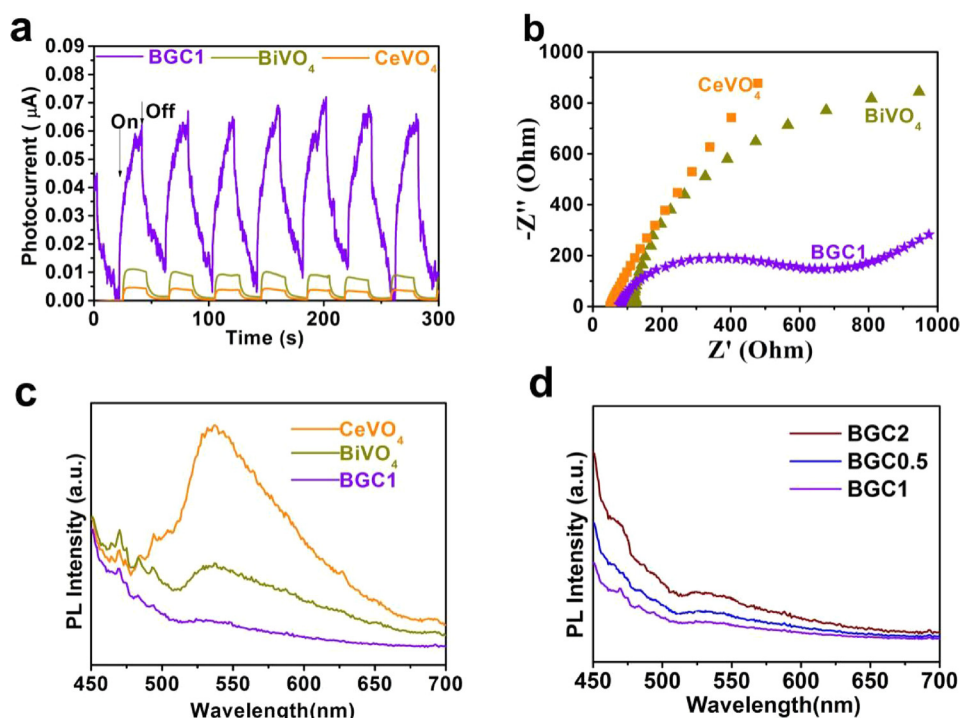
Fig. 8. (a) Photocurrent and (b) EIS of BiVO$_4$, CeVO$_4$ and the BCG1 composite electrodes under visible light irradiation, (c–d) PL spectra of as-prepared catalysts.

process in the presence of CeVO$_4$, BiVO$_4$ and BGC1 composite as pho-tocatalysts (Fig. 10b). For BiVO$_4$, the transformation percentage of NBT can be neglected, indicating that there is almost no ·O$_2^-$ production from the electrons. To further identify the radicals produced in photo-reaction process more intuitively, the DMPO spin-trapping ESR spectra

were carried out. Fig. 10c and d shows ESR signals of DMPO-·O$_2^-$ and DMPO-·OH of BiVO$_4$ and the BGC1 composite. It is obvious that no ESR signal was observed in dark, implying the importance of light illumi-nation. For the BGC1 composite, characteristic peaks of both DMPO-·O$_2^-$ and DMPO-·OH adducts with strong intensities can be observed
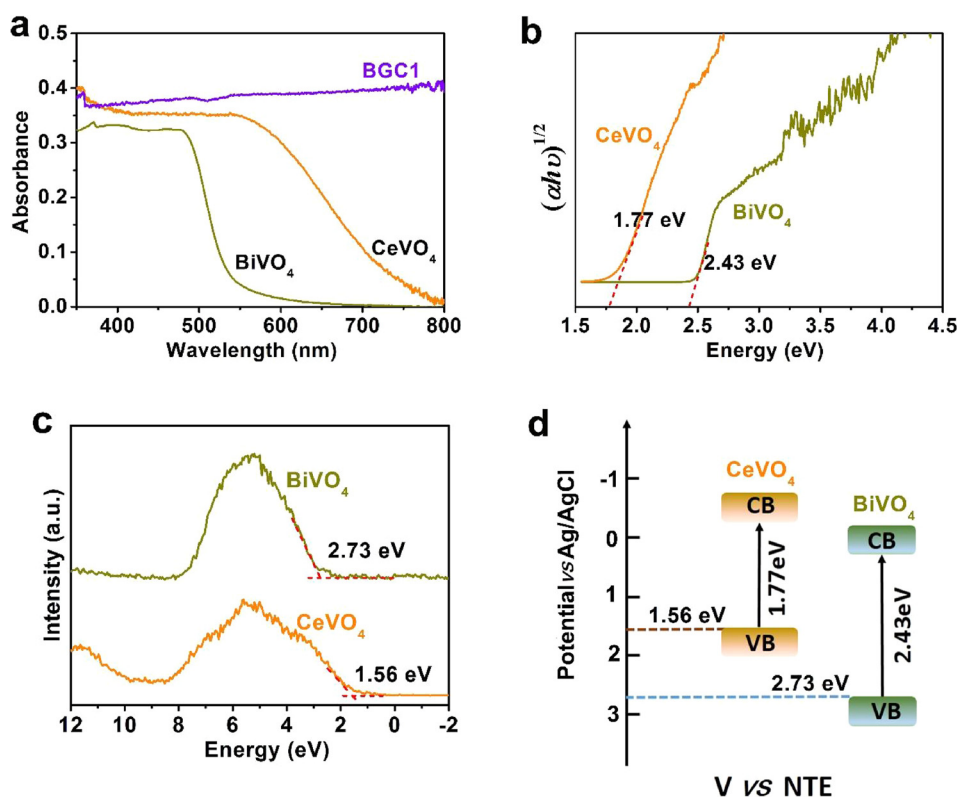

Fig. 9. (a) UV–vis diffuse reflectance spectra, (b) band gap values calculated from (αhν)$^{1/2}$ versus photon-energy plot, (c) valence band XPS spectra and (d) proposed band positions of BiVO$_4$, CeVO$_4$ in the BGC1 composite.
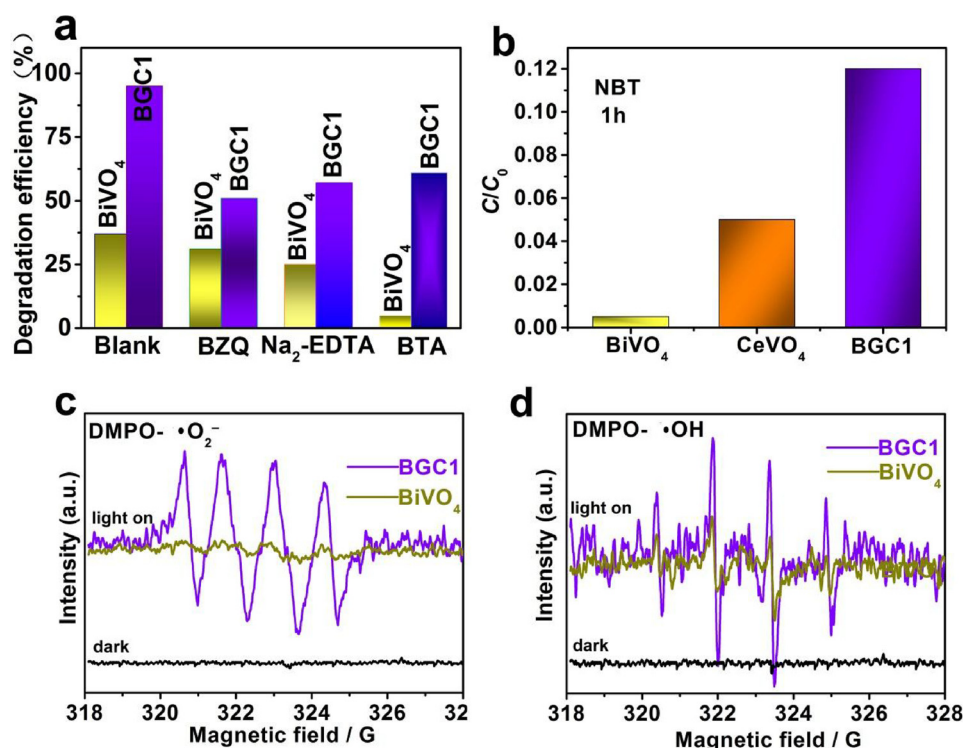
Fig. 10. (a) Holes and radicals trapping experiment results and (b) NBT transformation during the photocatalytic degradation toward TC over $CeVO_4$, $BiVO_4$ and the BGC1 composite; ESR spectra derived from illuminated $BiVO_4$ and the BGC1 composite recorded in (c) methanol and (d) H_2O dispersions, respectively.

insitu photocatalytic process. However, for bare $BiVO_4$, negligible signals derived from DMPO-$\cdot O_2^-$ radicals can be detected while four characteristic peaks of the DMPO-$\cdot OH$ adducts can be seen, indicating almost no $\cdot O_2^-$ species is produced after irradiation and $\cdot OH$ radicals are the main active species in the photocatalytic process. It is conclusive from the ESR analysis that active oxygen-containing radicals generating from the illuminated BGC composite are different from those derived from irradiated $BiVO_4$, $\cdot O_2^-$ and $\cdot OH$ radicals are considered as the main oxygen active species in-situ formed in the irradiated BGC1 composite, whereas the $\cdot OH$ radicals are believed to be the main oxygen active species originating from the illuminated $BiVO_4$.

Based on all of the aforementioned results, a more plausible explanation for the enhanced solar-driven photocatalytic performance of $BiVO_4$/3D RGO aerogel/$CeVO_4$ composite photocatalyst is proposed and possible pathways of charge transfer and redox reactions are schematically described in Fig. 11. Under visible light irradiation, both $BiVO_4$ and $CeVO_4$ could easily produce photo-induced electron-hole pairs due to their narrow band gaps. In a conventional heterostructure mechanism, $CeVO_4$ has a more negative CB potential and less positive VB level than those of $BiVO_4$, photogenerated electrons are transferred from the CB of $CeVO_4$ to CB of $BiVO_4$. Meanwhile, the holes in VB of $BiVO_4$ migrate to the VB of $CeVO_4$ (Fig. 11a). However, if the assumption is reasonable, the electrons accumulate on the CB level of $BiVO_4$ with a more positive potential than the redox potential of $\cdot O_2^-/O_2$ (-0.046 eV, NHE) [42,43], on the other hand, holes move to the VB of $CeVO_4$ with a less positive potential than the redox potential of $\cdot OH/OH^-$, both oxidation and reduction reactions are unable to occur, the generation of active $\cdot O_2^-$ and $\cdot OH$ radicals could not be fulfilled in this pathway. However, such results do not match our previous free radical test results. For the above reasons, a Z-scheme-type mechanism is proposed and the charge transfer process is suggested as shown in Fig. 11b. Contrast to conventional heterojunction mechanism, photogenerated electrons from CB of $BiVO_4$ may recombine with holes from the VB of $CeVO_4$ through the bridge of conductive 3D RGO skeleton, the carrier recombination processes of sole semiconductor is distinctly

hampered, and the electron-hole separation is accumulated by the specific tandem charge transportation channel. Due to the fact that the CB potential of $CeVO_4$ is more negative than the redox potential of $\cdot O_2^-/O_2$, $\cdot O_2^-$ can be produced by photo-induced electrons left on the CB position of $CeVO_4$. While holes remained in the VB position of $BiVO_4$ are active for the water oxidation. A Z-scheme-type photocatalytic mechanism is suggested where a highly efficient tandem pathway for electron transfer and charge transportation is constructed with an emphasis on the use of a flexible 3D RGO aerogel network as the solid-state electron mediator.

4. Conclusions

In summary, a novel synthetic approach has been demonstrated to fabricate $CeVO_4$/3D RGO aerogel/$BiVO_4$ ternary composites with well-defined nanostructures and enhanced interfacial contact. It is the first time that the ternary hybrid materials of two vanadates and 3D RGO aerogel has been prepared, the specific 3D intraconnected heterostuctures with abundant pores and active catalytic sites offer superior advantages in the adsorption and photodegradation of TC, as well as LED-illuminated oxygen production from water splitting. The oxygen-evolving efficiency and TC removal capability toward the optimal ternary composite BGC1 is 2.1 times, 3.7 times than those of $BiVO_4$ under visible light irradiation. The key role of 3D RGO aerogel as an effective solid-state electron mediator has been revealed in the irradiation Z-scheme photocatalytic composite systems. The Z-scheme configuration of 3D RGO aerogel-bridged vanadate semiconductors is proposed to be responsible for the enhanced light utilization, more efficient electron-hole separation and improved photocatalytic performance. This work provides a promising approach to the design and fabrication of highly efficient visible-light-responsive Z-scheme photocatalytic composite materials for energy and environmental applications.
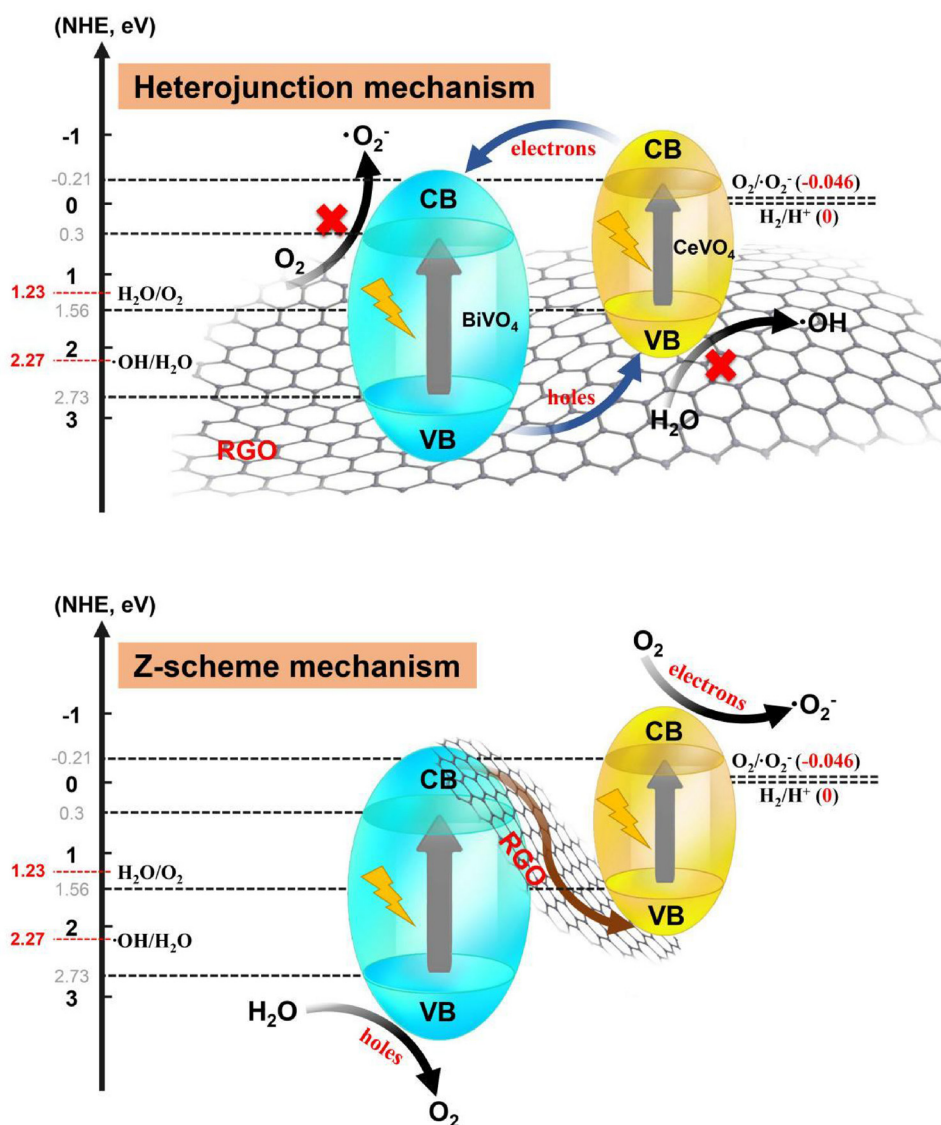
Fig. 11. Schematic illustration of proposed photocatalytic mechanism of the tandem $BiVO_4/RGO/CeVO_4$ ternary composite.

Acknowledgements

References

[1] X. Chen, Q. Chen, W. Jiang, Z. Wei, Y. Zhu, Appl. Catal. B Environ. 211 (2017) 106–113.

[2] H. Yu, R. Shi, Y. Zhao, T. Bian, Y. Zhao, C. Zhou, G.I.N. Waterhouse, L.Z. Wu, C.H. Tung, T. Zhang, Adv. Mater. 29 (2017) 1605148–1605155.

[3] R. Shi, Y. Cao, Y. Bao, Y. Zhao, G.I.N. Waterhouse, Z. Fang, L.Z. Wu, C.H. Tung, Y. Yin, T. Zhang, Adv. Mater. 29 (2017) 1700803–1700810.

[4] J. Low, J. Yu, M. Jaroniec, S. Wageh, A.A. Al-Ghamdi, Adv. Mater. 29 (2017) 1601694–1601714.

[5] Y. Wang, W. Yang, X. Chen, J. Wang, Y. Zhu, Appl. Catal. B Environ. 220 (2018) 337–347.

[6] X. Yang, H. Tang, J. Xu, M. Antonietti, M. Shalom, ChemSusChem 8 (2015) 1350–1358.

[7] X. Yang, Z. Chen, J. Xu, H. Tang, K. Chen, Y. Jiang, ACS Appl. Mater. Interfaces 7 (2015) 15285–15293.

[8] G. Yang, D. Chen, H. Ding, J. Feng, J.Z. Zhang, Y. Zhu, S. Hamid, D.W. Bahnemann, Appl. Catal. B Environ. 219 (2017) 611–618.

[9] B. Zhu, P. Xia, Y. Li, W. Ho, J. Yu, Appl. Surf. Sci. 391 (2017) 175–183.

[10] P. Zhou, J. Yu, M. Jaroniec, Adv. Mater. 26 (2014) 4920–4935.

[11] Y. Sasaki, A. Iwase, H. Kato, A. Kudo, J. Catal. 259 (2008) 133–137.

[12] J. Low, C. Jiang, B. Cheng, S. Wageh, A.A. Al-Ghamdi, J. Yu, Small Methods 1 (2017) 1700080–1700101.

[13] B. Feng, Z. Wu, J. Liu, K. Zhu, Z. Li, X. Jin, Y. Hou, Q. Xi, M. Cong, P. Liu, Q. Gu, Appl. Catal. B Environ. 206 (2017) 242–251.

[14] A. Iwase, S. Yoshino, T. Takayama, Y.H. Ng, R. Amal, A. Kudo, J. Am. Chem. Soc. 138 (2016) 10260–10264.

[15] A. Iwase, Y.H. Ng, Y. Ishiguro, A. Kudo, R. Amal, J. Am. Chem. Soc. 133 (2011) 11054–11057.

[16] K. Iwashina, A. Iwase, Y.H. Ng, R. Amal, A. Kudo, J. Am. Chem. Soc. 137 (2015) 604–607.

[17] X. Zeng, Z. Wang, G. Wang, T.R. Gengenbach, D.T. McCarthy, A. Deletic, J. Yu, X. Zhang, Appl. Catal. B Environ. 218 (2017) 163–173.

[18] W.K. Jo, N.C.S. Selvam, Chem. Eng. J. 317 (2017) 913–924.

[19] D. Ma, J. Wu, M. Gao, Y. Xin, Y. Sun, T. Ma, Chem. Eng. J. 313 (2017) 1567–1576.

[20] C. Lv, J. Sun, G. Chen, Y. Zhou, D. Li, Z. Wang, B. Zhao, Appl. Catal. B Environ. 208 (2017) 14–21.

[21] F. Chen, Q. Yang, X. Li, G. Zeng, D. Wang, C. Niu, J. Zhao, H. An, T. Xie, Y. Deng, Appl. Catal. B Environ. 200 (2017) 330–342.

[22] L. Li, H. Wang, X. Wang, Solid State Commun. 269 (2018) 11–15.

[23] Y. Fan, W. Ma, D. Han, S. Gan, X. Dong, L. Niu, Adv. Mater. 27 (2015) 3767–3773.

[24] Q.Q. Liu, C.Y. Fan, H.Tang T.D. Ma, J.Y. Shen, RSC Adv. 6 (2016) 85779–85786.

[25] C. Fan, Q. Liu, T. Ma, J. Shen, Y. Yang, H. Tang, Y. Wang, J. Yang, Ceram. Int. 42

(2016) 10487–10492.

[26] F. Chen, W. An, L. Liu, Y. Liang, W. Cui, Appl. Catal. B Environ. 217 (2017) 65–80.

[27] Y. Deng, L. Tang, G. Zeng, J. Wang, Y. Zhou, J. Wang, J. Tang, L. Wang, C. Feng, J. Colloid Interface Sci. 509 (2018) 219–234.

[28] T. Hirata, A. Watanabe, J. Solid State Chem. 158 (2001) 254–259.

[29] Z. Yue, A. Liu, C. Zhang, J. Huang, M. Zhu, Y. Du, P. Yang, Appl. Catal. B Environ. 201 (2017) 202–210.

[30] J. Yang, D. Chen, Y. Zhu, Y. Zhang, Y. Zhu, Appl. Catal. B Environ. 205 (2017) 228–237.

[31] S. Pu, R. Zhu, H. Ma, D. Deng, X. Pei, F. Qi, W. Chu, Appl. Catal. B Environ. 218 (2017) 208–219.

[32] X. Song, Y. Li, Z. Wei, S. Ye, D.D. Dionysiou, Chem. Eng. J. 314 (2017) 443–452.

[33] F. Chen, P. Ho, R. Ran, W. Chen, Z. Si, X. Wu, D. Weng, Z. Huang, C. Lee, J. Alloy Compd. 714 (2017) 560–566.

[34] Y.Z. Li, Q. Liu, X. Yang, H. Tang, Chinese J. Catal. 38 (2017) 2160–2170.

[35] C. Mu, Yu Zhang, W. Cui, Y. Liang, Y. Zhu, Appl. Catal. B Environ. 212 (2017)

41–49.

[36] K.Q. Lu, L. Yuan, X. Xin, Y.J. Xu, Appl. Catal. B Environ. 226 (2018) 16–22.

[37] L. Cui, X. Ding, Y. Wang, H. Shi, L. Huang, Y. Zuo, S. Kang, Appl. Surf. Sci. 391 (2017) 202–210.

[38] C. Cui, S. Li, Y. Qiu, H. Hu, X. Li, C. Li, J. Gao, W. Tan, Appl. Catal. B Environ. 200 (2017) 666–672.

[39] S. Cao, Q. Huang, B. Zhu, J. Yu, J. Power Sources 351 (2017) 151–159.

[40] H. Huang, X. Li, J. Wang, F. Dong, P.K. Chu, T. Zhang, Y. Zhang, ACS Catal. 5 (2015) 4094–4103.

[41] L. Yang, G. Dong, D.L. Jacobs, Y. Wang, L. Zang, C. Wang, J. Catal. 352 (2017) 274–281.

[42] P. Qiu, C. Xu, H. Chen, F. Jiang, X. Wang, R. Lu, Appl. Catal. B Environ. 206 (2017) 319–327.

[43] B. Wang, J. Di, P. Zhang, J. Xia, S. Dai, H. Li, Appl. Catal. B Environ. 206 (2017) 127–135.